CMS Physics Analysis Summary

Contact: cms-pag-conveners-susy@cern.ch 2012/03/10

Search for supersymmetry with the razor variables

The CMS Collaboration

Abstract

A search is performed for heavy particle pairs produced in $\sqrt{s} = 7$ TeV proton-proton collisions with ~ 4.4 fb^{-1} of data collected by the CMS experiment in 2011 at the CERN Large Hadron Collider. The search is sensitive to generic supersymmetry models provided superpartner particles are kinematically accessible, with minimal assumptions on properties of the lightest superpartner particle. The kinematic consistency of the selected events is tested against the hypothesis of heavy particle pair production using the dimensionless *razor* variable R, related to the missing transverse energy E_T^{miss}. The new physics signal is characterized by a broad peak in the distribution of M_R, an event-by-event indicator of the heavy particle mass scale. After background modeling based on data no significant deviation is observed from the Standard Model expectation. The results are interpreted in the context of the Constrained Minimal Supersymmetric Standard Model.

1 Introduction

Models with softly broken supersymmetry (SUSY) [1–5] predict superpartners of the standard model (SM) particles. Experimental limits from the Tevatron and LEP showed that superpartner particles, if they exist, are significantly heavier than their SM counterparts. Proposed experimental searches for R-parity conserving SUSY at the Large Hadron Collider (LHC) have therefore focused on a combination of two SUSY signatures: multiple energetic jets and/or leptons from the decays of pair-produced squarks and gluinos, and large missing transverse energy ($E_{\mathrm{T}}^{\mathrm{miss}}$) from the two weakly interacting lightest superpartners (LSP) produced in separate decay chains.

In this article we present results using the *razor* analysis framework that is inclusive not only for SUSY but also in the larger context of physics beyond the standard model. The focal point for the *razor* analysis [6, 7] is the production of pairs of heavy particles (of which squarks and gluinos are examples), whose masses are significantly larger than those of any SM particle. The analysis is designed to kinematically discriminate the pair production of heavy particles from SM backgrounds, without making strong assumptions about the $E_{\mathrm{T}}^{\mathrm{miss}}$ spectrum or details of the decay chains of these particles. The baseline selection requires two or more reconstructed objects, which can be calorimetric jets, isolated electrons or isolated muons. These objects are grouped into two *megajets*. The razor analysis tests the consistency, event by event, of the hypothesis that the two megajets represent the visible portion of the decays of two heavy particles. This strategy is complementary to traditional searches for signals in the tails of the $E_{\mathrm{T}}^{\mathrm{miss}}$ distribution [8–17] and is applied to data collected with the Compact Muon Solenoid (CMS) detector from pp collisions at $\sqrt{s} = 7\,\mathrm{TeV}$ corresponding to an integrated luminosity of $4.4\,\mathrm{fb}^{-1}$.

2 The CMS Apparatus

A description of the CMS detector can be found elsewhere [18]. A characteristic feature of the CMS detector is its superconducting solenoid magnet, of 6 m internal diameter, providing a field of 3.8 T. The silicon pixel and strip tracker, the crystal electromagnetic calorimeter (ECAL) and the brass/scintillator hadron calorimeter (HCAL) are contained within the solenoid. Muons are detected in gas-ionization chambers embedded in the steel return yoke. The ECAL has an energy resolution of better than 0.5 % above 100 GeV. The HCAL combined with the ECAL, measures the jet energy with a resolution $\Delta E/E \approx 100\,\%/\sqrt{E/\,\mathrm{GeV}} \oplus 5\,\%$.

CMS uses a coordinate system with the origin located at the nominal collision point, the x-axis pointing towards the center of the LHC, the y-axis pointing up (perpendicular to the LHC plane), and the z-axis along the counterclockwise beam direction. The azimuthal angle ϕ is measured with respect to the x-axis in the xy plane and the polar angle θ is defined with respect to the z-axis. The pseudorapidity is $\eta = -\ln[\tan(\theta/2)]$.

3 The Razor Analysis

The razor kinematics is based on the generic process of the pair production of two heavy particles, each decaying to an unseen particle plus jets. This includes SUSY signals with complicated and varied decay chains, or the simplest case of a pair of squarks each decaying to a quark and an LSP. All such processes are treated on an equal footing by forcing every event into a dijet topology; this is done by combining all jets in the event into two megajets. When an isolated lepton is present, it can be included in the megajets or not as explained in [7]. For the $1\ \mathrm{fb}^{-1}$ analysis the trigger requirements, pileup conditions, and pile-up subtraction dictate that iso-

lated electrons enter the megajet reconstruction as jets, while isolated muons are not included in the megajet reconstruction and mimic the contributions of neutrinos. The megajet reconstruction is thus based on a calorimeter-driven view of the events.

To the extent that the pair of megajets accurately reconstruct the visible portion of the underlying parent particle decays, the signal kinematics is equivalent to pair production of heavy squarks $\tilde{q}_1$, $\tilde{q}_2$, with $\tilde{q}_i \to \mathrm{j}_i\tilde{\chi}_i$, where the $\tilde{\chi}_i$ are LSPs and j_i denotes the visible products of the decays. For simplicity we will use the approximation that the j_i are massless.

The standard computation of the cross section for such a process uses a parameterization of the phase space and the matrix element extracted from consideration of three preferred reference frames: the rest frames of the two squarks and the center of mass (CM) frame.

In the rest frame of the ith squark, the 4-momenta of the squark and its decay products have the simple form

$$
\begin{aligned}
p_{\tilde{q}_i} &= M_{\tilde{q}}(1,0)\,, && (1)\\
p_{\mathrm{j}_i} &= \frac{M_\Delta}{2}(1,\hat{u}_i)\,, && (2)\\
p_{\chi_i} &= \frac{M_\Delta}{2}(\frac{1}{\beta_\Delta},-\hat{u}_i)\,, && (3)
\end{aligned}
$$

where the $\hat{u}_i$ are unit vectors in the directions of the visible decay products,

$$
M_\Delta \equiv \frac{M_{\tilde{q}}^2 - M_{\tilde{\chi}}^2}{M_{\tilde{q}}} = 2M_{\tilde{\chi}}\gamma_\Delta\beta_\Delta\,, \tag{4}
$$

and β_Δ is the boost parameter to the rest frame of the LSP $\tilde{\chi}_i$. The other preferred frame is the $\tilde{q}_1\tilde{q}_2$ CM frame, with

$$
\begin{aligned}
p_{\tilde{q}_1} &= \gamma_{CM}M_{\tilde{q}}\,(1,\,\beta_{CM}\hat{u}_{\tilde{q}})\,, && (5)\\
p_{\tilde{q}_2} &= \gamma_{CM}M_{\tilde{q}}\,(1,-\beta_{CM}\hat{u}_{\tilde{q}})\,, && (6)
\end{aligned}
$$

where $\hat{u}_{\tilde{q}}$ is a unit vector in the direction of the first squark, and β_{CM} is the boost parameter from the CM frame to the $\tilde{q}_1$ rest frame. In the CM frame the energies of the visible decay products can be written

$$
\begin{aligned}
E_{\mathrm{j}_1} &= \frac{\gamma_{CM}M_\Delta}{2}(1+\beta_{CM}\hat{u}_{\tilde{q}}\cdot\hat{u}_1)\,, && (7)\\
E_{\mathrm{j}_2} &= \frac{\gamma_{CM}M_\Delta}{2}(1+\beta_{CM}\hat{u}_{\tilde{q}}\cdot\hat{u}_2)\,. && (8)
\end{aligned}
$$

Since the second term typically averages to zero, the energy distribution for the visible decay products as measured in the CM frame peaks around $(\gamma_{CM}M_\Delta)/2$.

The problem with the conventional parameterization of this process is that, with two unseen LSPs, there are not enough experimental observables to reconstruct any of the three reference frames just described. This is true even in the absence of initial state p_T (as will now be assumed throughout), where the CM frame is just a longitudinal boost from the lab frame.

The strategy of the razor analysis is to approximate these unknown frames with a razor frame that is defined unambiguously from measured quantities in the lab frame. Event by event, razor frame observables then estimate the scales M_Δ and $\gamma_{CM}M_\Delta$ seen above.

A razor frame is defined by finding a longitudinal boost from the lab frame to a frame where the visible energies can be written in terms of an overall scale that is manifestly invariant under longitudinal boosts. This then defines a razor frame where the scale of the visible energies is set by a quantity that should approximate $\gamma_{CM}M_\Delta$ in the (unknown) CM frame. The longitudinal boost used here is defined as:

$$\beta_L^R \equiv \frac{p_z^{j_1} + p_z^{j_2}}{E_{j_1} + E_{j_2}} . \tag{9}$$

The razor boost β_L^R defines a frame where the visible four-momenta reduce to

$$p_{j_1} = (\frac{1}{2}(M_R - \frac{(\vec{p}_T^{\,j_1} - \vec{p}_T^{\,j_2}) \cdot \vec{E}_T^{miss}}{M_R}), p_T^{j_1}, p_z) , \tag{10}$$

$$p_{j_2} = (\frac{1}{2}(M_R + \frac{(\vec{p}_T^{\,j_1} - \vec{p}_T^{\,j_2}) \cdot \vec{E}_T^{miss}}{M_R}), p_T^{j_2}, -p_z) , \tag{11}$$

where M_R is the longitudinal boost invariant

$$M_R \equiv \sqrt{(E_{j_1} + E_{j_2})^2 - (p_z^{j_1} + p_z^{j_2})^2} , \tag{12}$$

and the longitudinal momentum p_z is determined from the massless on-shell conditions. This frame always exists since the magnitude of β_L^R is less than unity. This definition of M_R is enhanced with respect to the one used in [7] to avoid configurations where M_R is ill-defined due to unphysical Lorentz transformations. Here M_R as defined by (12) is an estimator of $\gamma_{CM}M_\Delta$.

The next step of the razor strategy is to define a transverse observable that can also serve as an event-by-event estimator of the underlying scale M_Δ. As usual for transverse quantities we expect M_Δ to be related to a kinematic edge rather than a peak.

Several choices of the transverse observable are plausible. To the extent that events match the assumed topology, the maximum value of the scalar sum of the megajets transverse momenta $(p_T^1,\ p_T^2)$ is M_Δ. The maximum value of the E_T^{miss} is also M_Δ. Especially useful is M_T^R, a kind of average transverse mass whose maximum value for signal events is also M_Δ:

$$M_T^R \equiv \sqrt{\frac{E_T^{miss}(p_T^{j1} + p_T^{j2}) - \vec{E}_T^{miss} \cdot (\vec{p}_T^{\,j1} + \vec{p}_T^{\,j2})}{2}} . \tag{13}$$

Given a global estimator M_R and a transverse estimator M_T^R, the razor dimensionless ratio is defined as

$$R \equiv \frac{M_T^R}{M_R} . \tag{14}$$

Signal events are characterized by the heavy scale M_Δ, while backgrounds are not. Qualitatively we expect M_R to peak for the signal over a steeply falling background. Thus the search

for an excess of signal events in a tail of a distribution is recast as a search for a peak on top of a steeply falling Standard Model residual tail.

To extract the peaking signal we need first to reduce the QCD multijet background to manageable levels. This is achieved by imposing a threshold value for R. For signal events M_T^R has a maximum value of M_Δ (i.e. a kinematic edge); thus R has a maximum value of approximately one and the distribution of R for signal peaks around 0.5, in contrast to QCD multijet events which peak at zero. These properties motivate the appropriate kinematic requirements for the signal selection and background reduction. We note that, while M_T^R and M_R measure the same scale (one as an end-point the other as a peak), they are largely uncorrelated for signal events [7].

4 Analysis path

In both simulation and data, the distributions of SM background events are seen to have a simple exponential dependence on the razor variables R and M_R over a large fraction of the R^2-M_R plane. The analysis uses simulated events to understand the shapes of the SM background distributions, the number of independent parameters needed to describe them, and extract initial estimates of the values of these parameters. For each of the main SM backgrounds, a control sample is then defined from a subset of the data that is dominated by this particular background in order to obtain a data-driven description of the shapes of the background components. A full SM background representation is thus built using statistically independent data samples; this is used as input for a global fit to the remaining data. The fit is performed in the corner of low M_R and small R^2; the distribution is then extrapolated on an orthogonal region of the R^2-M_R plane, defined such that the two regions overlap when projected on either one of the axes (R^2 or M_R). The fit includes parameters describing the shapes of the R^2-M_R distributions of the SM backgrounds as well as the relative fraction of each background.

The main steps in the analysis path are outlined below.

Definition of data samples

1. Inclusive data sets are collected with the electron, muon, and hadronic jet CMS triggers, multiobject triggers, and the suite of razor triggers (YR11) introduced in the CMS high level trigger menu in the spring of 2011.

2. These data sets are examined for the presence of a well-identified isolated electron or muon. Based on the presence or absence of such a lepton, the event is moved to one of the 6 disjoint event samples referred to as the electron (ELE), muon (MU), hadronic (HAD) and dilepton (MU-MU, ELE-ELE, MU-ELE) *boxes*. The dilepton boxes are hierarchical with the muon having priority over the electron (for example an $ee\mu$ event will go in the MU-ELE box and not in the ELE-ELE); the details are shown in Fig. 1. This hierarchy corresponds to an ordering of event samples from those with the less background population to those with more. Each of the five lepton boxes is further sub-divided according to the presence or absence of a b-tagged jet.

3. Three additional event samples are introduced to serve as data control samples for the QCD multijet background in the HAD, ELE, and MU boxes. The QCD multijet control sample for the HAD box is obtained from event samples recorded with pre-scaled jet triggers, while the QCD multijet control samples for the ELE and MU boxes are obtained by inverting the lepton isolation requirement.

4. Data control samples are defined dominated by $t\bar{t}$, Z+jets, and W+jets. These samples are obtained from non-razor-triggered data collected at the beginning of 2011 (NR11), amounting to approximately 200 pb^{-1} of integrated luminosity; this data is not used for the later stages of the analysis. For each box we obtain a top-enriched sample by requiring at least one b-tagged jet; simulated samples indicate that the shape of the R^2-M_R distributions are not biased by the b-tag requirement. The Z+jets enriched sample is the sum of the portions of the MU-MU and ELE-ELE boxes not containing a b-tag and and with dilepton invariant mass in the window between 60 and 120 GeV. The W+jets dominated sample is taken as the portions of the five lepton boxes not included in the $t\bar{t}$-dominated or Z+jets-dominated samples.

Initial determination of background shapes

1. Simulated samples are produced for the major SM backgrounds: QCD multijets, W+jets, Z+jets, and $t\bar{t}$, in all of the boxes (other SM backgrounds such as dibosons and single top are seen in simulation to make negligible contributions). The simulated samples are used to identify regions of the R^2-M_R plane in each box where the backgrounds can be described by simple exponentials. The parameters describing these exponential shapes in the simulated samples are extracted for each box and for each SM background, to be used as initial values in the fits to data control samples.

2. The R^2-M_R shape parameters are extracted from each data control sample in the exponential scaling regions as determined from the simulated samples. Two-dimensional maximum likelihood (ML) fits are performed for each of the relevant boxes that define the sample. Hence we obtain a preliminary description of the Standard Model background shapes, component by component, with combined statistical + systematic errors taken as the errors returned by the fits.

3. We observe that the exponential slopes for the second exponential component of all three major backgrounds (the second component being the one relevant at larger values of M_R-R^2) are all equal within the errors of the fits. This universality implies that a global fitting of the backgrounds for each box constrains the total yield as a function of R^2-M_R with a much smaller error than the error on the individual SM processes.

Final fitting and extrapolation to signal regions

1. The razor-triggered data is studied for each box in the R^2 –M_R plane. We apply a baseline requirement so that the triggers are fully efficient in the part of the R^2–M_R plane we use for the analysis. We also require $R^2 < 0.5$ to limit the analysis to the part of the plane where the exponential description of the background holds. These requirements define the *analysis region* in the R^2 –M_R plane for each box.

2. We define a *fit region* in the bottom-left corner of each analysis region (see Fig. 7 and Fig. 8). This region is dominated by SM processes, and we find in simulated samples that small signal contaminations have minor impact on the determination of the background shape. The rest of the analysis region is more sensitive to a potential SUSY signal.

3. We fit the events in the fit region for each box under the background-only hypothesis. The fit results from the data control samples provide initial values and constraints for these global fits, implemented by multiplying the likelihood by Gaussian penalty terms centered around these initial values. To avoid artificial differences in the second component

background composition extracted for each box, we assume a universal second component slope for the backgrounds in each box, while removing the Gaussian penalty for this parameter. Using the fits to the ELE and MU boxes we obtain the best precision on the second component of the background distribution. The fit second components output parameters are used as the second component input parameters to the other boxes, with a Gaussian penalty term derived from the MU box for the MU-MU and ELE-MU boxes, from the ELE box for the ELE-ELE box, and from both MU and ELE box for the HAD box applied (to the parameters of the second component). The projections of the results of the fits are shown in terms of the V+jets first component, the $t\bar{t}$+jets first component plus the effective standard model (V+jets and $t\bar{t}$+jets) second component for all the boxes, except for the HAD box where separate ELE-like and MU-like components are shown.

4. From the fit regions we have thus derived a model for the shape and yield of the SM background. We extrapolate the background model to the rest of the analysis region in the R^2 –M_R plane. We quantify the agreement between the data and the background model through the integral of the background model yield in a limited set of predefined non-overlapping *signal regions* (SRs) .

5. Observing no significant excess we proceed to set limits using a hybrid CL_s [19] test on the full R^2-M_R plane. We use a finer binning of the 2D plane to build a numerical pdf of the signal distribution for a given signal model.

Each of these steps is described in more detail later.

5 Monte Carlo Event Samples

The design of the analysis was guided by studies of Monte Carlo event samples generated with the PYTHIA6 [20] and MADGRAPH V4.22 [21] programs, simulated using the CMS GEANT-based [22] detector simulation, and then processed by the same software used to reconstruct real collision data. Events with QCD multijets, top quarks and electroweak bosons where generated with MADGRAPH interfaced with PYTHIA for parton showering, hadronization and the underlying event description. To generate Monte Carlo samples for SUSY the mass spectrum was first calculated with SOFTSUSY [23] and the decays with SUSYHIT [24]. The PYTHIA program was used with the SLHA interface [25] to generate the events. The generator level cross section and the k-factors for the Next-to-Leading Order (NLO) cross section calculation were computed using PROSPINO [26].

6 Event Selection

The analyses uses a set of dedicated triggers, which apply lower thresholds on the values of R and M_R, computed online from the reconstructed jets and missing energy. Three trigger categories are used: i) hadronic triggers, applying moderate/tight requirements on R and M_R to events with two jets of $p_T > 56$ GeV; ii) muon triggers, similar to the hadronic triggers, but with looser requirements on R and M_R and of at least one muon in the central part of the detector with $p_T > 10$ GeV iii) electron triggers, with similar R and M_R requirements and at least one electron of $p_T >$10 GeV, satisfying loose isolation criteria. All of these triggers are fully efficient in the kinematic regions used for this analysis. In addition, a set of non-razor pre-scaled and unprescaled triggers is used to define the control samples.

Events are required to have at least one good reconstructed interaction vertex [27]. When multiple vertices are found, the one with the highest associated $\sum_{track} p_T^2$ is used. Jets are reconstructed offline from calorimeter energy deposits using the infrared-safe anti-k_T [28] algorithm with radius parameter 0.5. Jets are corrected for the non-uniformity of the calorimeter response in energy and η using Monte Carlo and data derived corrections and are required to have $p_T > 60$ GeV and $|\eta| < 3.0$.

The jet energy scale uncertainty for these corrected jets is 5% [29]. The E_T^{miss} is reconstructed using the particle flow algorithm [30].

The electron and muon reconstruction and identification criteria are described in [31]. *Tight* electrons and muons are required to be isolated, within $|\eta| < 2.5$ and 2.1, respectively, and to satisfy the identification and selection requirements from [31]. *Loose* electron and muons have relaxed isolation requirements. The typical lepton trigger and reconstruction efficiencies are 98% and 99%, respectively, for electrons and 95% and 98% for muons.

The reconstructed hadronic jets and isolated electrons, and isolated muons are grouped into two megajets, when at least two such objects are present in the event. The megajets are constructed as a sum of the four-momenta of their constituent objects. After considering all possible partitions of the objects into two megajets, the combination minimizing the invariant masses summed in quadrature of the resulting megajets is selected among all combinations for which the R frame is well defined.

6.1 Box Classification

After the application of the baseline selection and calculation of the variables R and M_R, the remaining events are assigned to one final state box according to the isolated lepton content of the event. Six different boxes are considered in the analysis, corresponding to zero, one and two lepton final states, split according to lepton flavor (electrons and muons). The lepton p_T thresholds in the definition of the boxes are chosen such that the lepton triggers used to select events are approximately fully-efficient. The six boxes are

- ELE-MU Box: Events must contain at least one loose electron with $p_T > 20$ and at least one tight muon $p_T > 10$ GeV.
- MU-MU Box: Events must contain at least two loose muons with $p_T > 15$ GeV and $p_T > 10$ GeV, respectively of which one is tight muon with $p_T > 10$ GeV.
- ELE-ELE Box: Events must contain a loose electron with $p_T > 20$ GeV and at least one tight electron with $p_T > 10$ GeV.
- MU Box: Events must contain at least one tight muon with $p_T > 12$ GeV.
- ELE Box: Events must contain at least one loose electron with $p_T > 20$ GeV.
- HAD Box: Events must not satisfy any other box requirements.

In addition, for the leptonic boxes we require $M_R > 300$ GeV and $0.11 < R^2 < 0.5$, while for the hadronic box we require $M_R > 400$ GeV and $0.18 < R^2 < 0.5$. These requirements are the loosest possible compatible with the validity of the background description and the request of a fully-efficient trigger. They identify the *full region* of the R^2-M_R plane, where the analysis is performed.

In order to prevent ambiguities when an event satisfies the selection requirements of more than one box, the boxes are arranged in a predefined hierarchy. The decision to assign an event to a given box is evaluated in a preferential order, with an event being uniquely assigned to the first box whose criteria the event satisfies. The hierarchy and box classification procedure is

described in the flow-diagram of Fig. 1.

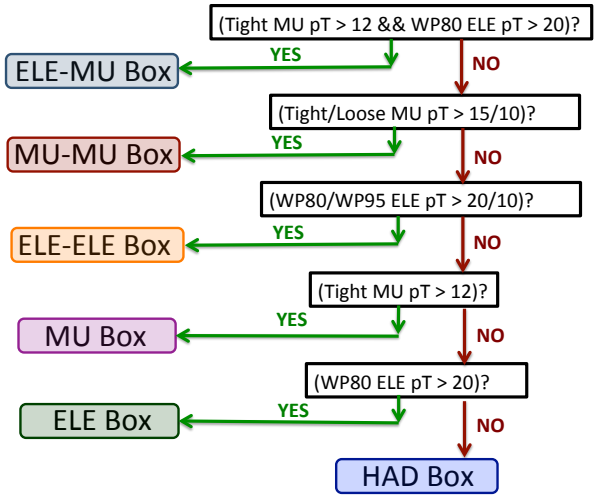

Figure 1: Flow diagram of box classification logic. The box selection proceeds according to a box hierarchy in order to ensure complete orthogonality of box selections and to resolve ambiguities when an event satisfies more than one box's selection criteria.

7 Backgrounds

In traditional searches for SUSY based on missing transverse energy, it is difficult to model the tails of the E_T^{miss} distribution, and the contribution from events with spurious instrumental effects. The QCD multijet production is an especially difficult background due to its large cross section and complicated modeling of the high p_T and E_T^{miss} tails. In this analysis a threshold on R makes it possible to remove the QCD multijet background.

Apart from the QCD multijet background, the remaining backgrounds in the lepton, dilepton and hadronic boxes are processes with genuine E_T^{miss} due to energetic neutrinos and leptons from massive vector boson decays, including W's from top quark decays and diboson production. After applying an R threshold, the M_R distributions in the single lepton, dilepton, and hadronic boxes are very similar for these backgrounds; this similarity is exploited in their modeling and normalization.

7.1 QCD multijet background

The QCD multijet control sample for the hadronic box is defined from event samples recorded with pre-scaled jet triggers and passing the baseline analysis selection for events without a well-identified isolated electron or muon. The trigger requires at least two jets with average uncorrected p_T thresholds of 60 GeV/c. The QCD multijet background dominates these samples for low M_R allowing the extraction of the M_R shapes with different R_{cut} thresholds for QCD multijet events.

The M_R distributions for events satisfying the QCD control box selection, for different values of the R_{cut} threshold, are shown in Fig. 2 (left). The M_R distribution is exponentially falling,

after a turn-on at low M_R resulting from the p_T threshold requirement on the jets entering the megajet calculation. The exponential region of these distributions is fitted for each value of R^2 to extract the coefficient in the exponent, denoted by S. The value of S that maximizes the likelihood in the exponential fit is found to be a linear function of R^2_{cut} as shown in Fig. 2 (right); fitting S in the form $S = a + bR^2_{\text{cut}}$ determines the values of a and b.

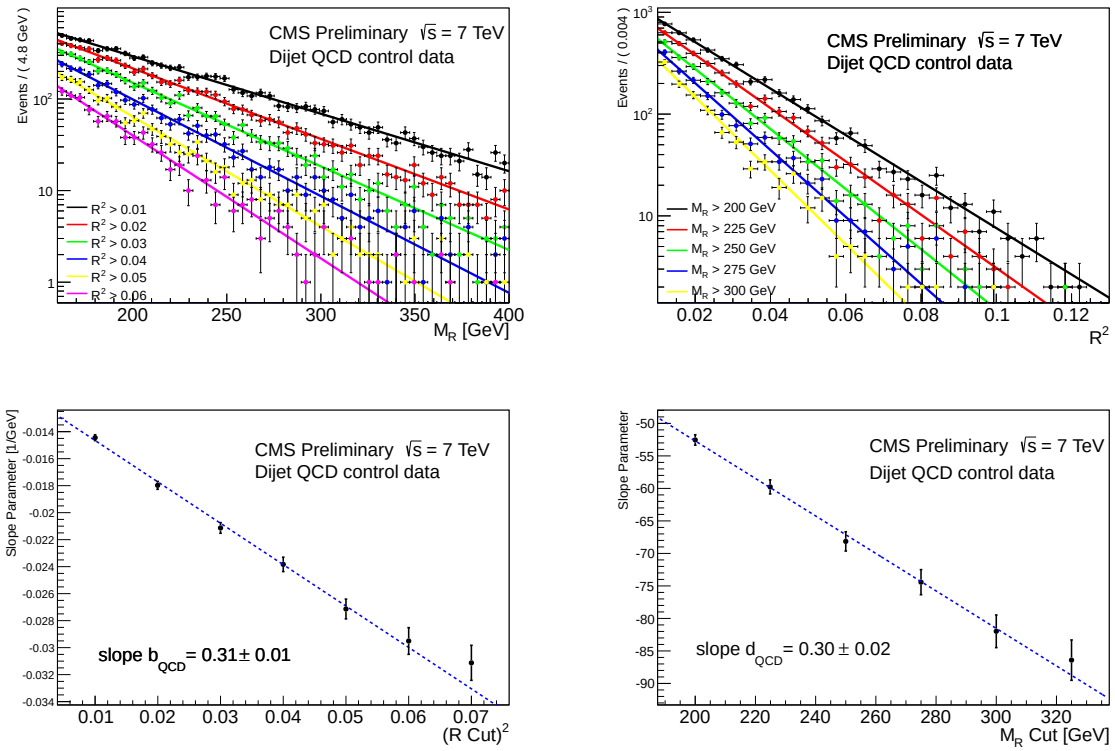

Figure 2: (Top left) M_R distributions for different values of the R^2 threshold for events in data selected in the QCD control box. (Top right) R^2 distributions for different values of the M_R threshold for events in data selected in the QCD control box. (Bottom left) The exponential slope S from fits to the M_R distribution, as a function of the square of the R^2 threshold for data events in the QCD control box. (Bottom right) The coefficient in the exponent S from fits to the R^2 distribution, as a function of the square of the M_R threshold for data events in the QCD control box.

The R^2_{cut} distributions for events satisfying the QCD control box selection, for different values of the M_R threshold, are shown in Fig. 2 (left). The R^2 distribution is exponentially falling, after a turn-on at low R^2. The exponential region of these distributions is fitted for each value of M_R^{cut} to extract the coefficient in the exponent, again denoted by S'. The value of S' that maximizes the likelihood in the exponential fit is found to be a linear function of M_R^{cut} as shown in Fig. 2 (right); fitting S' in the form $S' = c + dM_R^{\text{cut}}$ determines the values of c and d. The d slope parameter is found to equal the b slope parameter within an accuracy of a few percent as shown in Fig. 2. This is used in building a 2D probability density function (pdf) that analytically describes the R^2 vs M_R distribution and recovers an exponential distribution in $M_R(R^2)$ after integrating out $R^2(M_R)$, exploiting the equality $d = b$.

The other backgrounds exhibit the same behavior; each SM process can be described with the same functional form but different parameters.

7.2 W+jets, Z+jets and top+X backgrounds

7.2.1 MU and ELE boxes

In both simulated and data events in the muon (MU) and electron (ELE) boxes, the M_R distribution is well described with two independent exponential components. The first component of $W(\ell\nu)$+jets contains events where the electron or muon significantly contributes in the mega-jet reconstruction, and has a steeper slope compared to the second component. Both slopes along with their relative and absolute normalizations are simultaneously floated. The M_R distributions as a function of R^2 in the data are shown in Fig. 3 (top left) in the MU box with the requirement of 0 b-tagged jets. The slope parameters characterizing the exponential behavior of the 1^{st} $W(\mu\nu)$+jets and 2^{nd} components are shown in Fig. 3 (center,right). The values of $b1$ and $b2$ that describe the R^2 dependence of the slopes are in good agreement with the values extracted from simulated $W(\ell\nu)$+jets events as shown in the same figures (bottom).

The R^2 distributions as a function of M_R in the data are shown in Fig. 4 (top left) in the MU box with the requirement of 0 b-tagged jets. The slope parameters characterizing the exponential behavior of the 1^{st} $W(\mu\nu)$+jets and 2^{nd} components are shown in Fig. 4 (center,right). The values of $d1$ and $d2$ that describe the M_R dependence of the slopes are in good agreement with the values extracted from simulated $W(\ell\nu)$+jets events as shown in the same figures (bottom). Furthermore the extracted values of $d_1(d_2)$ are in agreement with the extracted values of $b_1(b_2)$.

7.2.2 Dilepton Boxes

The dilepton boxes are expected to be populated by the Z+jets candle events for the ELE-ELE, MU-MU boxes, and $t\bar{t}$ for these boxes and the MU-ELE box. In the 2010 analysis with 35 pb^{-1} these boxes were poorly populated, and the normalization of the Z+jets and $t\bar{t}$+jets backgrounds was performed using the W+jets and $t\bar{t}$+jets measured cross sections and the razor scaling in the ELE, MU boxes. In the current analysis the dilepton boxes are sufficiently populated by Z+jets candle events and $t\bar{t}$ events. The NR11 dataset collected before the deployment of the razor triggers is used to define control samples for these backgrounds.

We find the M_R distributions as a function of R^2 in the $t\bar{t}(2\ell 2\nu)$+jets MADGRAPH simulated events in the dilepton final states (ELE-ELE, MU-MU, MU-ELE) are independent of the lepton flavor combination. This background component is similar in all boxes and for its shape and normalization we use the same initial values.

8 Background Determination

We perform an extended and unbinned maximum likelihood (ML) fit, using the ROOFIT fitting tool [32]. For each box, the fit is performed in the portion of the R^2-M_R plane delimited by the green contours in Fig. 7 and Fig. 8. We refer to this region as the *fit region*. The fit provides a full description of the SM background in the R^2-M_R plane in each box. The likelihood function for a given box is written as [33]:

$$\mathcal{L}_b = \frac{e^{-(\sum_{j\in SM} N_j)}}{N!} \prod_{i=1}^{N} \Big(\sum_{j\in SM} N_j P_j(M_{R,i}, R_i^2) \Big) \,, \tag{15}$$

where N is the total number of events in the box; the sum runs on all the Standard Model processes relevant for that box, N_j is the yield of a given fit sample in the box, and $P_j(M_R, R^2)$ is the two-dimensional pdf describing the R^2 versus M_R distribution of the considered process.

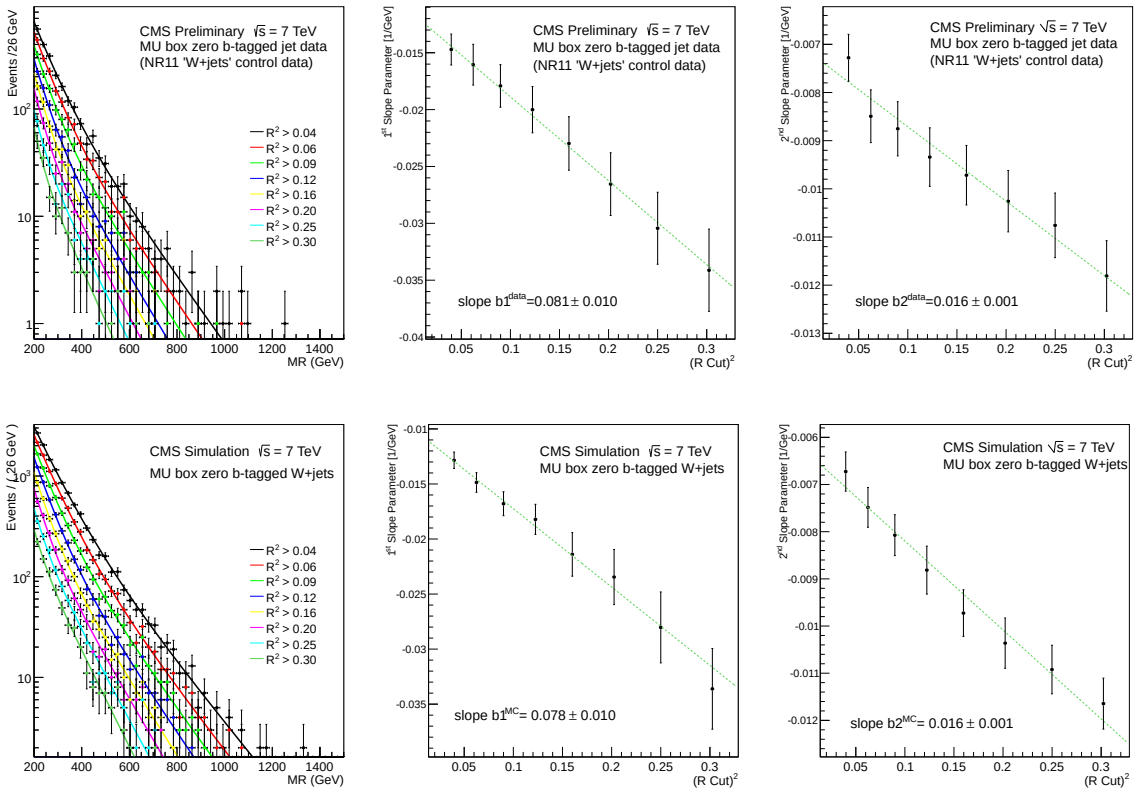

Figure 3: (Top left) M_R distributions for different values of the R^2 threshold for events in data selected in the MU box with the requirement of 0 b-tagged jets. The dotted lines show two independent exponential components fit to the the M_R distribution, (top center) value of the first exponential slope S from fits to the M_R distribution, as a function of the R^2 threshold (top right) value of the second exponential slope S from fits to the M_R distribution, as a function of the R^2 threshold. (Bottom) The corresponding in simulated W+jets events.

The P_j function is written as the sum of two instances of the same function (two *components*)

$$P_j(M_R, R^2) = (1 - f_2^j) \times F_j^{1st}(M_R, R^2) + f_2^j \times F_j^{2nd}(M_R, R^2)\,, \tag{16}$$

where f_2^j is the relative fraction of the second component and each component is written as:

$$F_j(M_R, R^2) = \left[k_j(M_R - M_{R,j}^0)(R^2 - R_{0,j}^2) - 1\right] e^{-k_j(M_R - M_{R,j}^0)(R^2 - R_{0,j}^2)}\,. \tag{17}$$

When integrated on M_R (R^2), this function recovers the exponential behavior on R^2 (M_R). The k_j parameters of the function are the same as the b and d parameters introduced in Section 7 that determine the scaling of the exponential constant as a function of the threshold on M_R and R^2. The identity $b = d$ is built into the functional form of Eq. 17.

While the shape of the first component is in general box dependent, the second component is found to be box independent in simulation studies as well as in fits to control data samples with either a b-tag requirement or a b-tag veto. This behavior is found to be associated with large initial state radiation (ISR).

To obtain the initial background shapes we parameterize the pdf of each process by using specific data control samples. For the QCD multijet background we use a set of pre-scaled

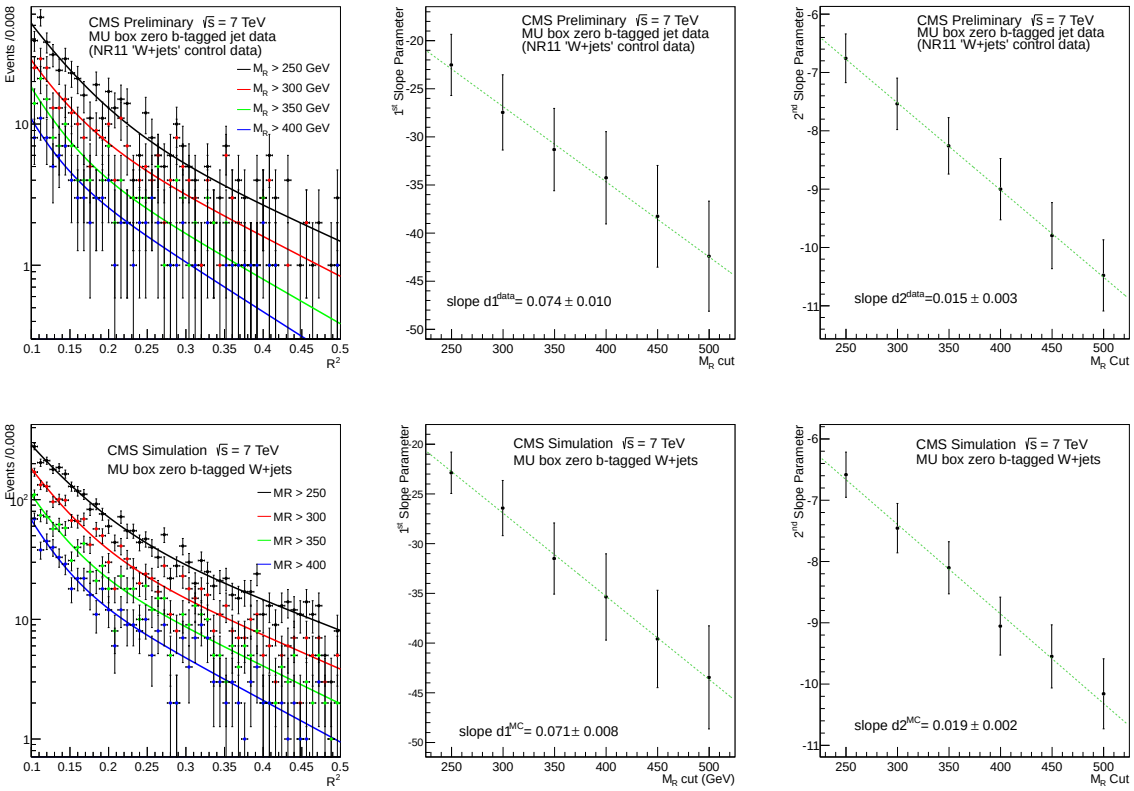

Figure 4: (Top left) R^2 distributions for different values of the M_R threshold for events in data selected in the MU box with the requirement of 0 b-tagged jets. The dotted lines show two independent exponential components fit to the the R^2 distribution, (top center) value of the first exponential slope S from fits to the R^2 distribution, as a function of the M_R threshold (top right) value of the second exponential slope S from fits to the R^2 distribution, as a function of the M_R threshold. (Bottom) The corresponding in simulated W+jets events.

single-jet triggers for the hadronic box. We invert the isolation (electron id) requirement in order to select a sample of *non-isolated muon* (*non-isolated electron*) events from the MU (ELE) box as discussed in detail in [7].

For $t\bar{t}$ we use non-razor trigerred control datasets in the five leptonic and dileptonic boxes, requiring at least one b-tagged jet. This sample is about 90% pure, as estimated from simulation studies. We neglect the residual contamination, mainly due to W+jets events. These $t\bar{t}$ control samples are simultaneously fitted, enforcing the universality of the second component.

Similarly, we use non-razor triggered control datasets in the four leptonic and same-flavor dileptonic boxes requiring 0 b-tagged jets to describe the W+jets and Z+jets background. The shape parameters (those of Eq. 16 and 17) are determined for each box through the 2D fit. Gaussian penalty terms are imposed for the parameters k_j, $M^0_{R,j}$ and $R^2_{0,j}$; the penalty terms for the k_j parameters are typically $\sim$30%.

The result of the fits to the data control samples are used as initial values for the 2D fits in each of the boxes. The uncertainties on the shape parameters, extracted from the data control sample fits, are used as the σ of the penalty terms multiplying the likelihood.

The values of the shape parameters that maximize the likelihood in these fits, along with the

corresponding covariance matrix, are used to define the background model and the uncertainty associated to it.

Once this parameterization is determined, it is used to estimate the total SM background yield in regions where a SUSY or other new physics signal would be visible. In the absence of such a signal, the background shape is used to constrain the parameters of the new physics model under consideration.

We perform the fit to the background shapes in the regions delimited by the green dashed lines in Fig. 7 and Fig. 8. The result of the ML fit projected on M_R and R^2 is shown in Fig. 5 for the dilepton boxes and Fig 6 for the MU, ELE and HAD boxes. No significant discrepancy is observed between the data and the fit model.

9 Signal Regions

In order to establish the compatibility of the background model to the observed dataset, we define a set of signal regions (SR) on the tail of the background distribution.

The SR are chosen before looking at the data, based on the prediction of the background model obtained by Monte Carlo simulation. The SR are defined such that full range of M_R values (after the event selection) is covered. Different requirements on R^2 are used in different SR, such that the expected background yield is kept small. The defined SR are shown in Fig. 7 (for MU-MU, MU-ELE, and ELE-ELE boxes) and Fig. 8 (for MU, ELE, and HAD).

Using the background model returned by the ML fit, we derive the distribution of the expected yield in each SR using pseudo-experiments.

In order to correctly account for correlations and uncertainties on the parameters describing the background model, the shape parameters used to generate each pseudo-experiment dataset are sampled from the covariance matrix returned by the ML fit. The actual number of events in each dataset is then drawn from a Poisson distribution centered on the yield returned by the covariance-matrix sampling. For each pseudo-experiment dataset, the number of events in the SR is found. For each of the SR, the distribution of the number of events derived by the pseudo-experiments is used to calculate a two-sided p-value, corresponding to the probability of observing an equal or less probable outcome for a counting experiment in each SR. The p-values obtained are quoted in Fig. 7 and Fig. 8. In the same figures, we quote the median and the mode of the yield distribution for each SR, together with the observed yield. A 68% probability interval is also calculated, using the probability associated to each yield outcome as the ordering principle.

No significant deviation is observed, which indicates the compatibility of the background model to the data and the absence of a significant excess from non-SM processes.

10 Interpretation of the Results

We interpret our result as an exclusion limit at 95% confidence level (CL) in the m_0 versus $m_{1/2}$ plane of the CMSSM parameter space for $\tan\beta = 10$, $A_0 = 0$, and positive μ.

We scan the CMSSM parameter space in the the $m_{1/2}$ versus m_0 plane and perform a hypothesis test. There are two well-specified situations under consideration: either the background only hypothesis (H_0) is enough to model the data, or we must include a signal component (H_1) in order to correctly model the distribution seen in data. In the absence of a significant deviation

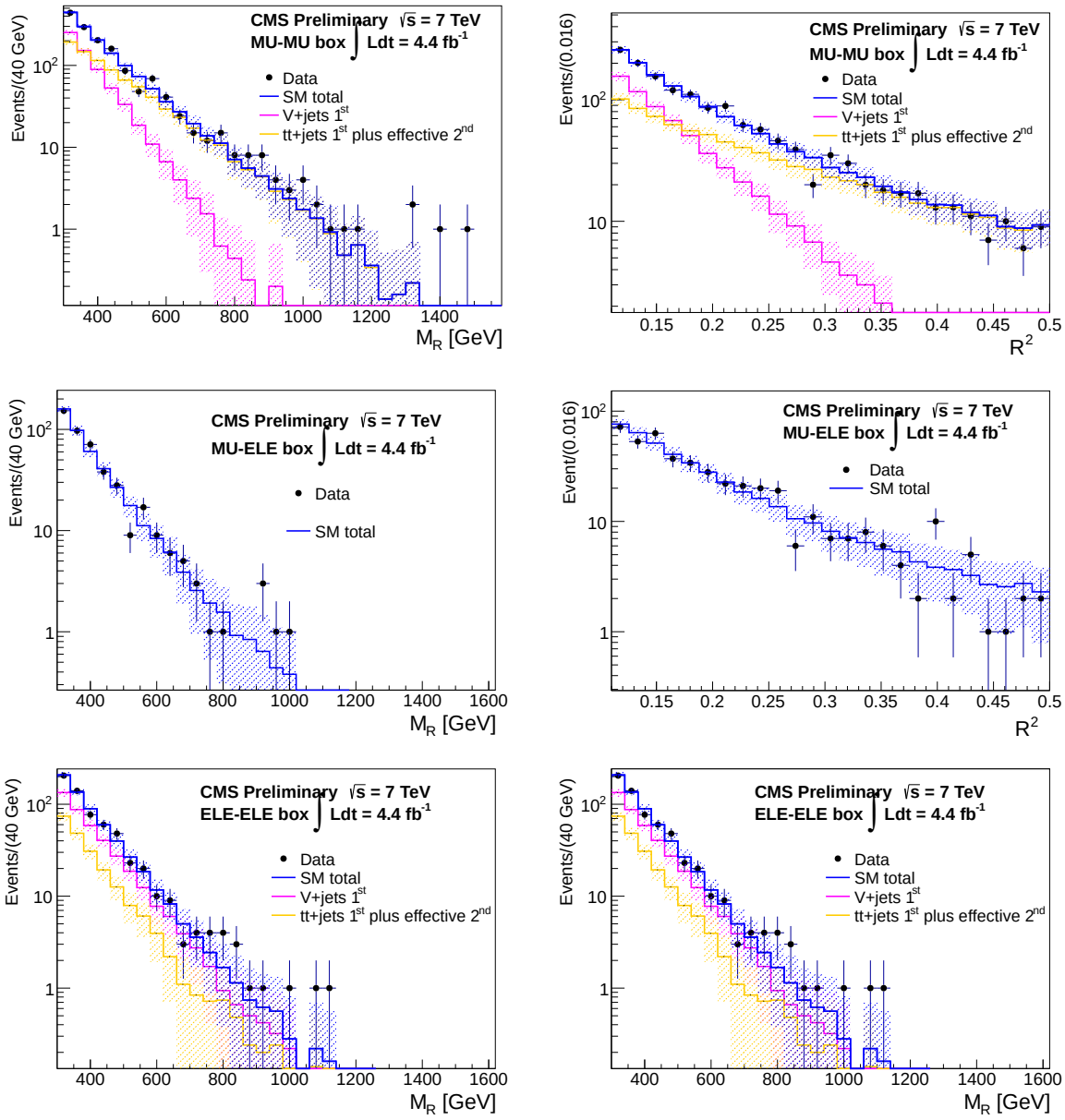

Figure 5: Projection of the 2D fit result on M_R (left) and R^2 (right) for the MU-MU, MU-ELE and ELE-ELE boxes using the razor datasets.The blue histogram is the total Standard Model prediction as obtained from a single pseudo-experiment based on the 2D fit. The magenta and yellow histograms show the breakdown of the Standard Model prediction into two separate components as returned by the fit. The fit is performed in the R^2-M_R sideband and projected into the full region. Only the statistical error on the total SM background prediction is shown in these projecions. In the MU-ELE box case the total Standard Model background is dominated by the second effective component contribution.

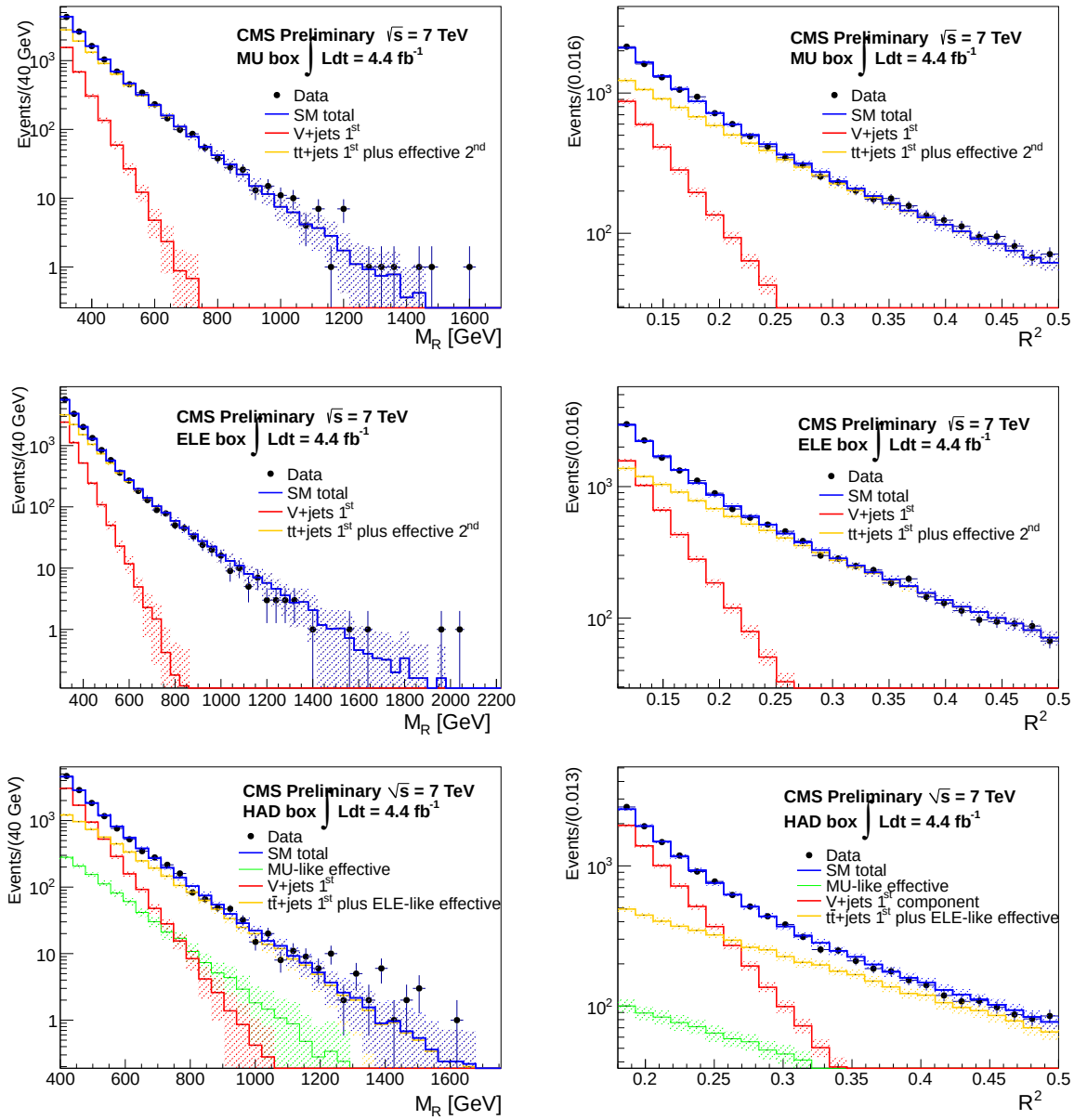

Figure 6: Projection of the 2D fit result on M_R (left) and R^2 (right) for the MU (top), ELE (center), HAD (bottom) boxes in the YR11 dataset. The blue histogram is the total Standard Model prediction as obtained from a single pseudo-experiment based on the 2D fit. The green, red, and yellow histograms show the breakdown of the Standard Model prediction into separate components as returned by the fit. The fit is performed in the R^2-M_R sideband (as an example the magenta dotted line in the HAD box projection on M_R denotes the corresponding fit region) and projected into the full region. Only the statistical error on the total SM background prediction is shown in these projections.

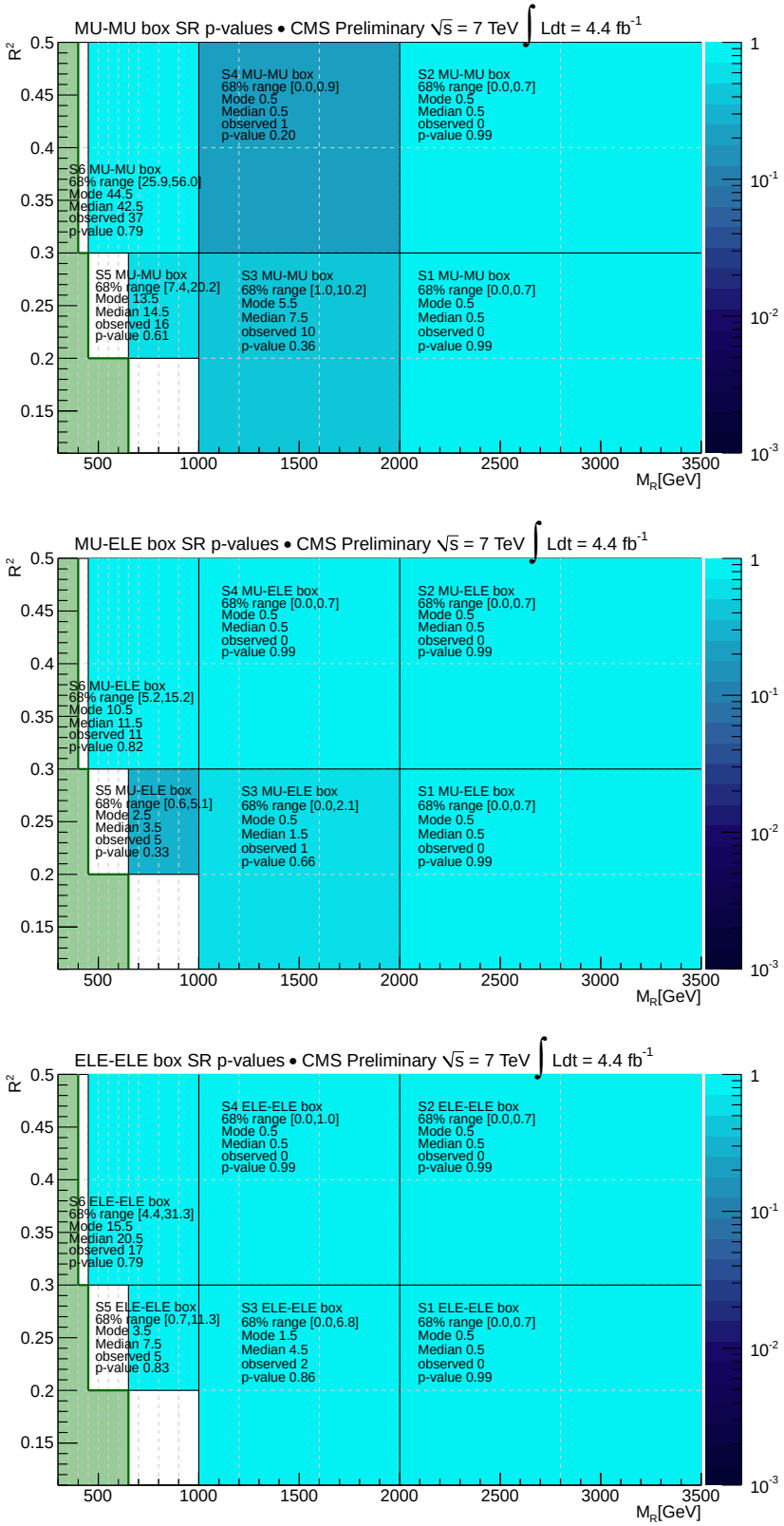

Figure 7: The p-values corresponding to the observed number of events in the MU-MU (top), MU-ELE (center), and ELE-ELE (bottom) box signal regions defined for this analysis. The green regions indicate the fit regions. The p-values test the compatibility of the observed number of events in data with the SM expectation (obtained from the background parameterization).

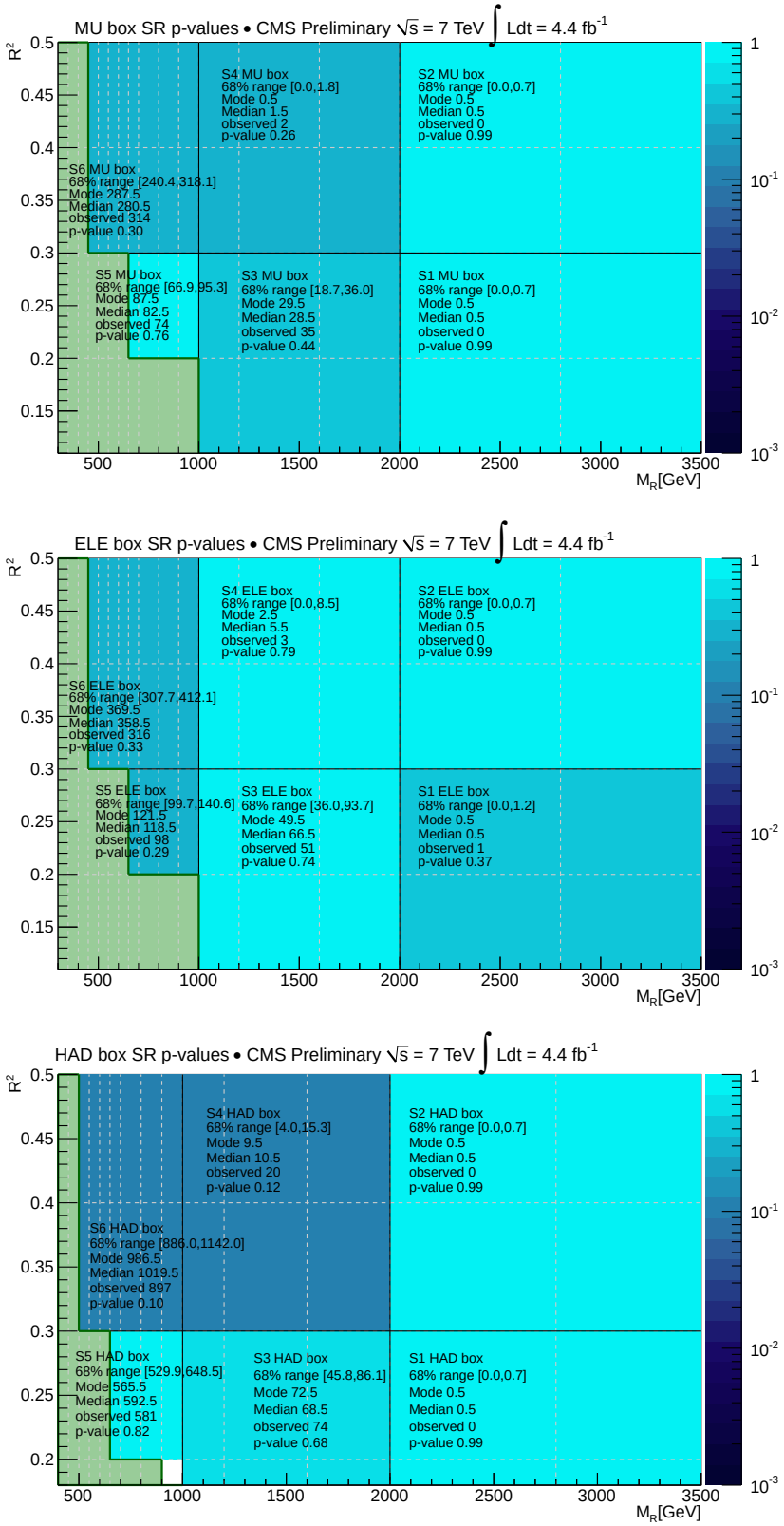

Figure 8: The p-values corresponding to the observed number of events in the MU (top), ELE (middle), and HAD (bottom) box signal regions defined for this analysis. The green regions indicate the fit regions. The p-values test the compatibility of the observed number of events in data with the SM expectation (obtained from the background parameterization).

from our background model, we associate a CL to the rejection of H_1 in favor of H_0, computing the value of the hybrid CL_s [19] for that model point.

Each hypothesis is represented as a likelihood function. The hypothesis H_0 is associated to the likelihood function of Eq. 15, while the likelihood function associated to H_1 is written as:

$$\mathcal{L}_{s+b} = \frac{e^{-N_S-(\sum_{j\in SM} N_j)}}{N!} \prod_{i=1}^{N} (N_S P_S(M_{R,i}, R_i^2) + \sum_{j\in SM} N_j P_j(M_{R,i}, R_i^2)) \,, \tag{18}$$

where the background parameters N_j and the pdf's $P_j(M_R, R^2)$ are the same as in Eq. 15; N_S is the expected signal yield, and $P_S(M_R, R^2)$ is the pdf associated to the model-point, parameterized as a 2D template function using Monte Carlo simulation. We use variable binning in M_R to further avoid sparse signal pdfs at larger M_R. The value of N_S in each box is computed from the NLO cross section of the considered model point, the nominal luminosity value corresponding to the dataset, and the reconstruction efficiency for the considered model point, evaluated using Monte Carlo simulation. In leptonic boxes, the shape and normalization of the signal pdf is corrected for the data–simulation agreement on the efficiency of the lepton selection, as determined with a tag-and-probe study performed on a sample of reconstructed $Z \to \ell\ell$ decays ($\ell = e, \mu$) in bins of p_T and η.

For each box we consider the test statistics given by the logarithm of the likelihood ratio $\ln Q = \ln \frac{\mathcal{L}(s+b|H)}{\mathcal{L}(b|H)}$, where H is the hypothesis under test H_1 (signal plus background) or the null hypothesis H_0 (background-only). For a given dataset, we evaluate $\ln Q$ in the full region of events passing the baseline selection, excluding only the events belonging to the *fit region*. These box-specific test statistics are combined in a total discriminant, writing the total likelihood as the product of the likelihoods of each box. This implies that the combined value for $\ln Q$ is given by $\ln Q_{TOT} = \Sigma_{box} \ln Q_{box}$.

Assuming the validity of H_0, the distribution of $\ln Q$ is derived from an ensemble of background-only pseudo-experiments, following the same procedure as described in Sec. 9.

We determine the distribution of $\ln Q$ under the assumption of H_1 by sampling pseudo-experiment datasets out of the likelihood function of Eq. 18. As for the background-only pseudo-experiments, the background model for each generation is derived from the covariance matrix returned by the ML fit. Similarly, the signal pdf is varied *at generation* in each pseudo-experiment, in order to take into account the systematic error associated to the normalization and the shape of the signal distribution. We consider effects across the R^2– M_R plane that coherently affect the overall normalization, as well as systematic effects that vary across the R^2–M_R plane and between final state boxes which can affect the signal pdf shape. Bin-by-bin, the total systematic error on the $P_S(M_R, R^2)$ function of Eq. 18 is the convolution of the individual effects each modeled with a log-normal function. The systematic effects on the signal yield and the the signal shape modeling are summarized in Table 1. We consider variations of the function modeling the signal uncertainty (log-normal vs Gaussian) as well as the binning finding negligible deviations in the result.

While the systematic uncertainties are included when sampling the pseudo-experiments, the likelihood values are computed taking the nominal values for the shape and normalization parameters for both the background and signal pdf's.

Given the distribution of $\ln Q$ for background-only and signal-plus-background pseudo-experiments, the value of $\ln Q$ observed in the data $\ln Q^{\text{data}}$ determines the two tail regions of Fig. 9, the integral of which yields the values of CL_{s+b} and $1 - CL_b$. From these values we compute

$CL_s = CL_{s+b}/CL_b$. These CL_s values are used to set a limit in the CMSSM plane, excluding models at 95% CL if $CL_s < 0.05$. The inclusive result is shown in Figure 10. We use the template of [34]. We also present the results of the HAD box (Figure 11), the lepton boxes (Figure 12) and the overlay of the above (Figure 13).

l

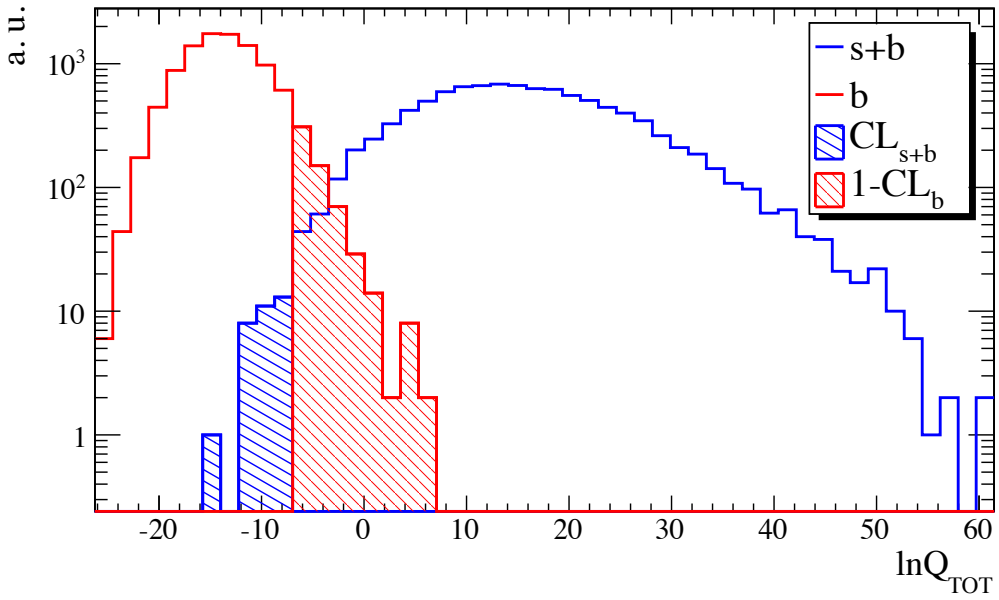

Figure 9: Distribution of $\ln Q_{TOT}$ for background-only (left) and signal+background (right) pseudo-experiments, corresponding to a CMSSM model with $A_0 = 0$, positive sign of μ, $\tan\beta = 10$, $m_0 = 1000$ GeV, and $m_{1/2} = 305$ GeV. Here, the subscript TOT indicates that all six final state boxes are used in constructing the test statistic. The value $\ln Q^{\text{data}}_{TOT} = -8.55$ observed on data delimits the CL_s and $1 - CL_b$ tails, shown as hatched regions in the figure.

Table 1: Summary of the systematic uncertainties on the signal yield and shape.

yield systematics	
$\mathcal{L}$[35]	4.5%
cross section	point-by-point
trigger efficiency R^2-M_R	2%
trigger efficiency lepton	3% (lepton, dilepton boxes)
shape systematics	
PDF	point-by-point (up to 30%)
JES	point-by-point (up to 1%)
lepton-id (tag-and-probe)	1% (per lepton)

11 Summary

We performed a search for squarks and gluinos using a data sample of $\sim$4.4 fb^{-1} integrated luminosity from pp collisions at $\sqrt{s} = 7$ TeV, recorded by the CMS detector at the LHC. The kinematic consistency of the selected events was tested against the hypothesis of heavy particle

pair production using the dimensionless razor variable R related to the missing transverse energy $E_{\mathrm{T}}^{\mathrm{miss}}$, and M_R, an event-by-event indicator of the heavy particle mass scale.

In a control dataset we find a simple 2D functional form that describes the distributions of the relevant SM backgrounds as a function of R^2 and M_R. This function is proved to model the correlation between R^2 and M_R in the region under study to a good precision in the Monte Carlo, much higher than the precision of the fit used to predict the shape of the backgrounds from data. Assuming the modeling of the R^2 vs M_R implied by the 2D function is correct, a 2D fit of the R^2 and M_R distributions in control regions is used to predict the background yields and shapes in regions at high mass scale that could contain events from new physics.

No significant excess over the background expectations was observed and the results were presented as a 95% CL in the (m_0, $m_{1/2}$) CMSSM parameter space. We exclude up to 1.35 TeV squarks and gluinos for $m(\tilde{q}) \sim m(\tilde{g})$ and for $m(\tilde{q}) > m(\tilde{g})$ we exclude gluinos up to 800 GeV.

These results significantly extend the current LHC limits.

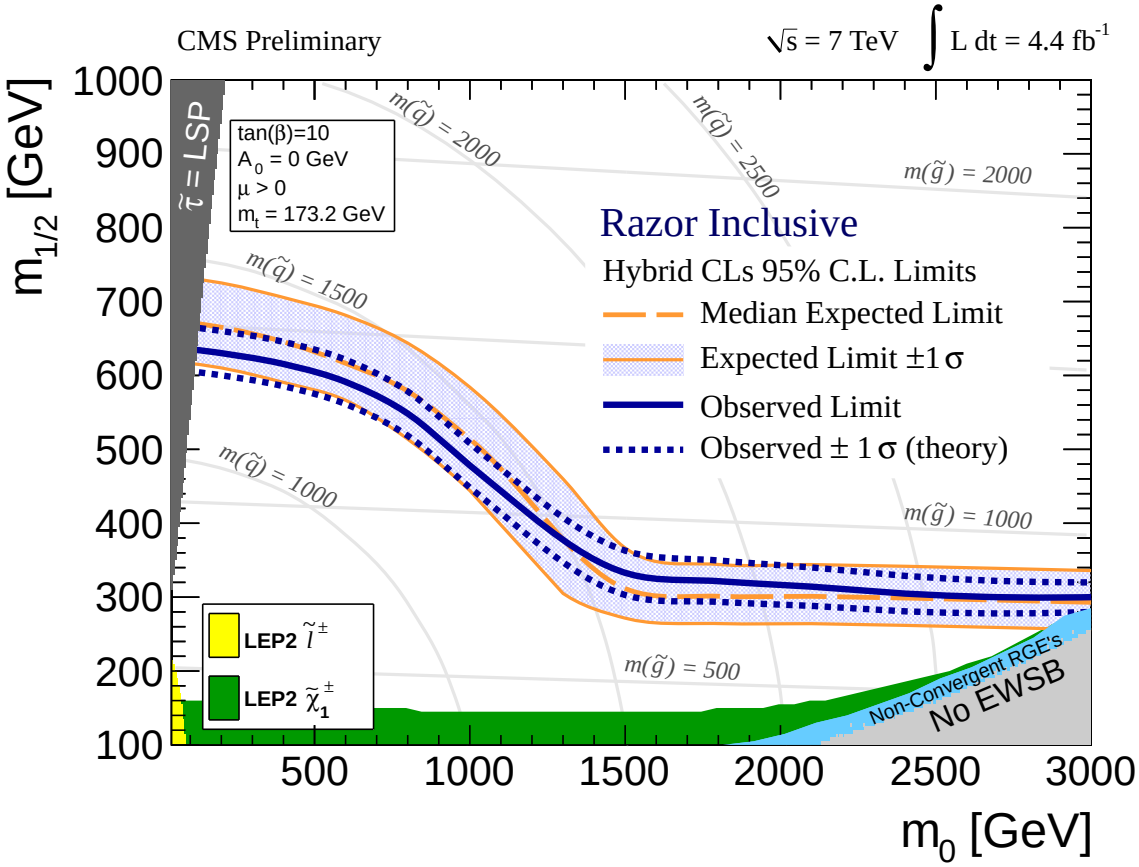

Figure 10: Observed (solid curve) and median expected (dot-dashed curve) 95% CL limits in the (m_0, $m_{1/2}$) CMSSM plane with $\tan\beta = 10$, $A_0 = 0$, $\mathrm{sgn}(\mu) = +1$ from the razor analysis. The $\pm$ one standard deviation equivalent variations in the uncertainties are shown as a band around the median expected limit.

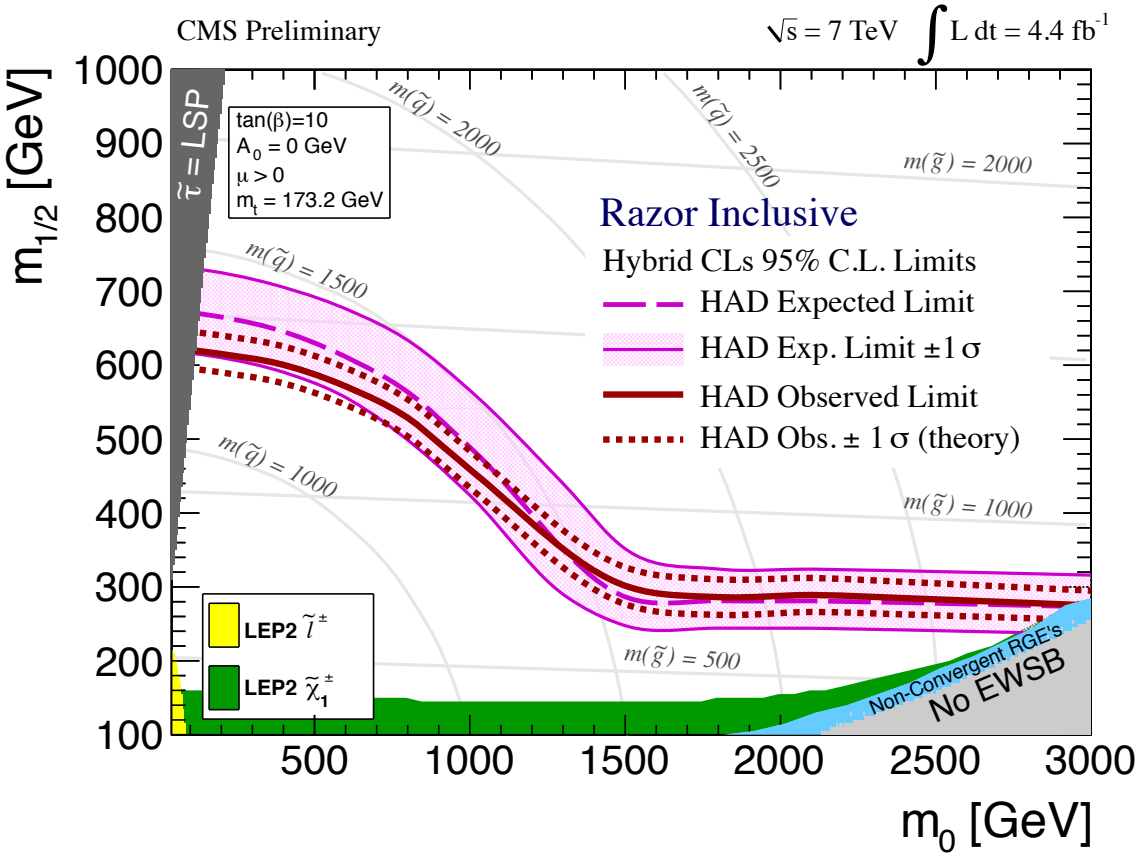

Figure 11: Observed (solid curve) and median expected (dot-dashed curve) 95% CL limits in the (m_0, $m_{1/2}$) CMSSM plane with $\tan\beta = 10$, $A_0 = 0$, $\mathrm{sgn}(\mu) = +1$ from the razor HAD box analysis. The $\pm$ one standard deviation equivalent variations in the uncertainties are shown as a band around the median expected limit.

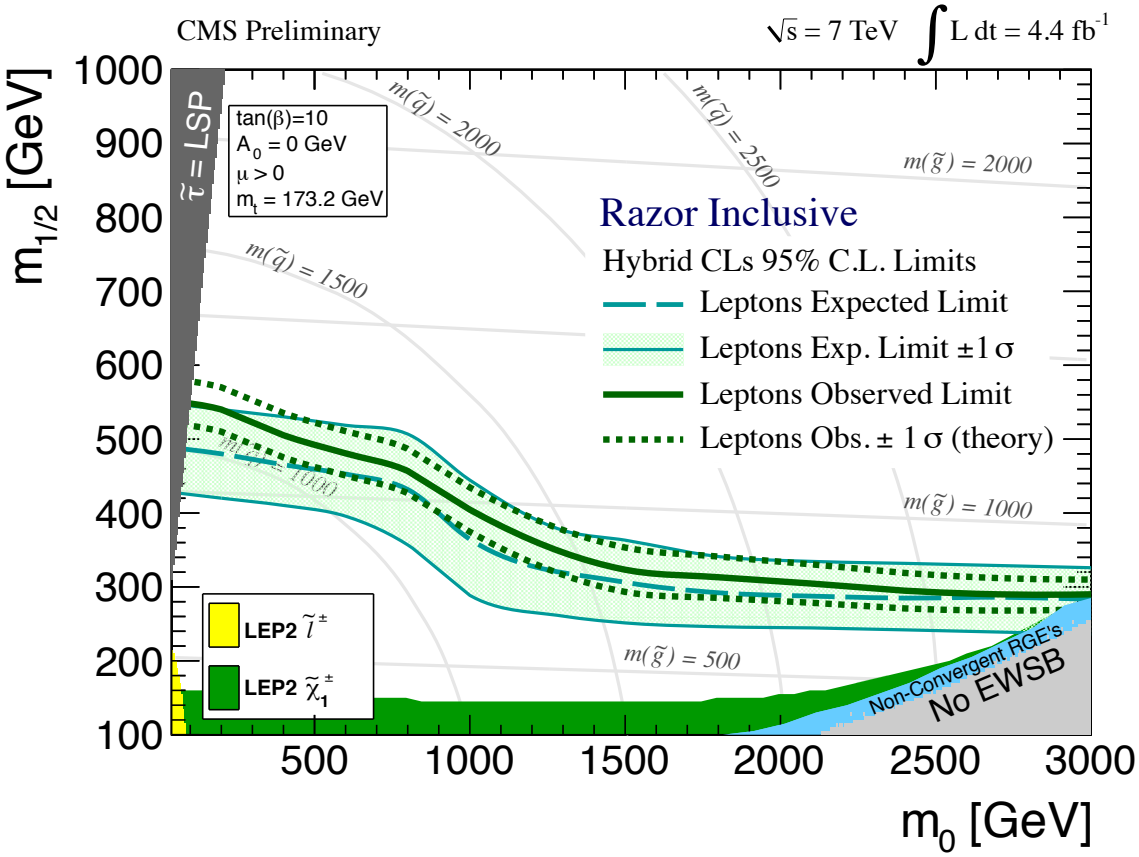

Figure 12: Observed (solid curve) and median expected (dot-dashed curve) 95% CL limits in the (m_0, $m_{1/2}$) CMSSM plane with $\tan\beta = 10$, $A_0 = 0$, $\mathrm{sgn}(\mu) = +1$ from the razor leptonic boxes analysis. The $\pm$ one standard deviation equivalent variations in the uncertainties are shown as a band around the median expected limit.

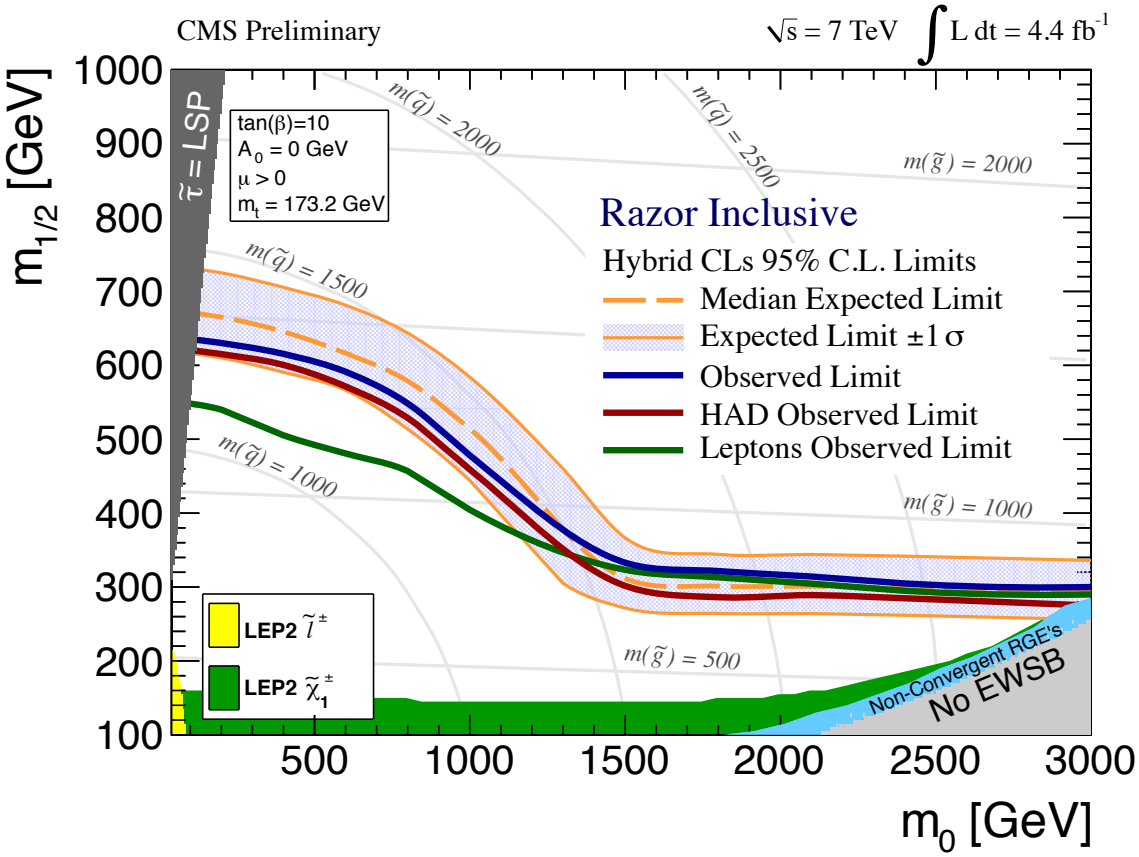

Figure 13: Observed (solid blue curve) and median expected (dot-dashed curve) 95% CL limits in the $(m_0, m_{1/2})$ CMSSM plane with $\tan\beta = 10$, $A_0 = 0$, $\mathrm{sgn}(\mu) = +1$ from the razor analysis. The $\pm$ one standard deviation equivalent variations in the uncertainties are shown as a band around the median expected limit. Shown separately the observed HAD-only (solid crimson) and leptonic-only (solid green) 95% CL limits.

References

[1] P. Ramond, "Dual Theory for Free Fermions", *Phys. Rev.* **D3** (1971) 2415–2418. doi:10.1103/PhysRevD.3.2415.

[2] Y. Golfand and E. Likhtman, "Extension of the Algebra of Poincare Group Generators and Violation of p Invariance", *JETP Lett.* **13** (1971) 323–326.

[3] D. Volkov and V. Akulov, "Possible universal neutrino interaction", *JETP Lett.* **16** (1972) 438–440.

[4] J. Wess and B. Zumino, "Supergauge Transformations in Four-Dimensions", *Nucl. Phys.* **B70** (1974) 39–50. doi:10.1016/0550-3213(74)90355-1.

[5] P. Fayet, "Supergauge Invariant Extension of the Higgs Mechanism and a Model for the Electron and Its Neutrino", *Nucl. Phys.* **B90** (1975) 104–124. doi:10.1016/0550-3213(75)90636-7.

[6] C. Rogan, "Kinematics for new dynamics at the LHC", arXiv:1006.2727. CALT-68-2790.

[7] CMS Collaboration, "Inclusive search for squarks and gluinos in pp collisions at sqrt(s) = 7 TeV", *Phys. Rev. D.* **85** (2012) arXiv:1107.1279.

[8] D0 Collaboration, "Search for squarks and gluinos in events with jets and missing transverse energy using 2.1 fb^{-1} of p anti-p collision data at $s^{(1/2)}$ = 1.96 TeV", *Phys. Lett.* **B660** (2008) 449–457, arXiv:0712.3805. doi:10.1016/j.physletb.2008.01.042.

[9] CDF Collaboration, "Inclusive Search for Squark and Gluino Production in p anti-p Collisions at $s^{(1/2)}$ = 1.96 TeV", *Phys. Rev. Lett.* **102** (2009) 121801, arXiv:0811.2512. doi:10.1103/PhysRevLett.102.121801.

[10] ATLAS Collaboration, "Search for an excess of events with an identical flavour lepton pair and significant missing transverse momentum in $\sqrt{s}$= 7 TeV proton-proton collisions with the ATLAS detector", (2011). arXiv:1103.6208. Accepted by EPJC.

[11] Atlas Collaboration, "Search for squarks and gluinos using final states with jets and missing transverse momentum with the ATLAS detector in sqrt(s) = 7 TeV proton-proton collisions", arXiv:1102.5290.

[12] Atlas Collaboration, "Search for supersymmetry using final states with one lepton, jets, and missing transverse momentum with the ATLAS detector in sqrt(s) = 7 TeV pp", arXiv:1102.2357.

[13] ATLAS Collaboration, "Search for supersymmetric particles in events with lepton pairs and large missing transverse momentum in $\sqrt{s}$ = 7 TeV proton-proton collisions with the ATLAS experiment", (2011). arXiv:1103.6214. Accepted by EPJC.

[14] CMS Collaboration, "Search for new physics with the jets and missing momentum signature at the LHC", *CMS PAS* **SUS-10-005** (2011).

[15] CMS Collaboration, "Search for Supersymmetry in pp Collisions at 7 TeV in Events with Jets and Missing Transverse Energy", *Phys. Lett.* **B698** (2011) 196–218, arXiv:1101.1628. doi:10.1016/j.physletb.2011.03.021.

[16] CMS Collaboration, "Search for new physics with same-sign isolated dilepton events with jets and missing transverse energy at the LHC", arXiv:1104.3168.

[17] CMS Collaboration, "Search for Physics Beyond the Standard Model in Opposite- Sign Dilepton Events at sqrt(s) = 7 TeV", arXiv:1103.1348.

[18] CMS Collaboration, "The CMS experiment at the CERN LHC", *JINST* **3** (2008) S08004. doi:10.1088/1748-0221/3/08/S08004.

[19] A. L. Read, "Presentation of search results: The CL(s) technique", *J.Phys.G* **G28** (2002) 2693–2704. doi:10.1088/0954-3899/28/10/313.

[20] T. Sjöstrand, S. Mrenna, and P. Skands, "PYTHIA 6.4 Physics and Manual; v6.420, tune D6T", *JHEP* **05** (2006) 026, arXiv:hep-ph/0603175.

[21] F. Maltoni and T. Stelzer, "MadEvent: Automatic event generation with MadGraph", *JHEP* **02** (2003) 027, arXiv:hep-ph/0208156.

[22] GEANT4 Collaboration, "GEANT4: A simulation toolkit", *Nucl. Instrum. Meth.* **A506** (2003) 250–303. doi:10.1016/S0168-9002(03)01368-8.

[23] B. C. Allanach, "SOFTSUSY: a program for calculating supersymmetric spectra", *Comput. Phys. Commun.* **143** (2002) 305–331, arXiv:hep-ph/0104145. doi:10.1016/S0010-4655(01)00460-X.

[24] A. Djouadi, M. M. Muhlleitner, and M. Spira, "Decays of Supersymmetric Particles: the program SUSY-HIT (SUspect-SdecaY-Hdecay-InTerface)", *Acta Phys. Polon.* **B38** (2007) 635–644, arXiv:hep-ph/0609292.

[25] P. Z. Skands et al., "SUSY Les Houches Accord: Interfacing SUSY Spectrum Calculators, Decay Packages, and Event Generators", *JHEP* **07** (2004) 036, arXiv:hep-ph/0311123. doi:10.1088/1126-6708/2004/07/036.

[26] W. Beenakker, R. Hopker, and M. Spira, "PROSPINO: A program for the PROduction of Supersymmetric Particles In Next-to-leading Order QCD", arXiv:hep-ph/9611232.

[27] CMS Collaboration, "Tracking and Primary Vertex Results in First 7 TeV Collisions", *CMS PAS* **TRK-10-005** (2010).

[28] M. Cacciari, G. P. Salam, and G. Soyez, "The anti-kt jet clustering algorithm", *JHEP* **0804** (2008) 063–074. doi:10.1088/1126-6708/2008/04/063.

[29] CMS Collaboration, "Determination of the Jet Energy Scale in CMS with pp Collisions at sqrt(s) = 7 TeV", *CMS PAS* **JME-10-010** (2010).

[30] CMS Collaboration, "Commissioning of the Particle-Flow Reconstruction in Minimum-Bias and Jet Events from pp Collisions at 7 TeV", *CMS PAS* **PFT-10-002** (2010).

[31] CMS Collaboration, "Measurements of Inclusive W and Z Cross Sections in pp Collisions at 7 TeV", *CMS PAS* **EWK-10-002** (2010).

[32] W. Verkerke and D. P. Kirkby, "The RooFit toolkit for data modeling", arXiv:physics/0306116.

[33] R. J. Barlow, "Extended maximum likelihood", *Nucl.Instrum.Meth.* **A297** (1990) 496–506. doi:10.1016/0168-9002(90)91334-8.

[34] K. Matchev and R. Remington, "Updated templates for the interpretation of LHC results on supersymmetry in the context of mSUGRA", arXiv:1202.6580.

[35] CMS Collaboration, "Absolute luminosity normalization", *CMS DPS* **CERN-CMS-DP-2011-002** (2011).